

New hot subdwarf stars identified in Gaia DR2 with LAMOST DR5 spectra

ZHENXIN LEI,^{1,2} JINGKUN ZHAO,¹ PÉTER NÉMETH,^{3,4} AND GANG ZHAO¹

¹Key Laboratory of Optical Astronomy, National Astronomical Observatories, Chinese Academy of Sciences, Beijing 100012, China

²College of Science, Shaoyang University, Shaoyang 422000, China

³Astronomical Institute of the Czech Academy of Sciences, CZ-251 65, Ondřejov, Czech Republic

⁴Astroserver.org, 8533 Malomsok, Hungary

(Received ; Revised; Accepted)

Submitted to

ABSTRACT

We selected 4593 hot subdwarf candidates from the Gaia DR2 Hertzsprung-Russell (HR) diagram. By combining the sample with LAMOST DR5, we identified 294 hot subdwarf stars, including 169 sdB, 63 sdOB, 31 He-sdOB, 22 sdO, 7 He-sdO and 2 He-sdB stars. The atmospheric parameters (e.g., T_{eff} , $\log g$, $\log(n\text{He}/n\text{H})$) are obtained by fitting the hydrogen (H) and helium (He) line profiles with synthetic spectra. Two distinct He sequences of hot subdwarf stars are clearly presented in the $T_{\text{eff}}-\log g$ diagram. We found that the He-rich sequence consists of the bulk of sdB and sdOB stars as well as all of the He-sdB, He-sdO and He-sdOB stars in our samples, while all the stars in the He-weak sequence belong to the sdO spectral type, combined with a few sdB and sdOB stars. We demonstrated that the combination of Gaia DR2 and LAMOST DR5 allows one to uncover a huge number of new hot subdwarf stars in our Galaxy.

Keywords: (stars:) HertzsprungRussell and CM diagrams, (stars:) subdwarfs, surveys:Gaia,

1. INTRODUCTION

Hot subdwarf stars consist of O and B type stars (spectral type sdO, sdB and related objects) at a late stellar evolution stage (Heber 2009, Heber 2016). These stars have low stellar masses (e.g., about $0.5M_{\odot}$) and burn helium (He) in their cores or evolve off this evolution stage. Hot subdwarf stars present very high effective temperatures (e.g., $T_{\text{eff}} \geq 20000$ K) due to their thin hydrogen (H) envelopes ($< 0.01M_{\odot}$, Heber 2016) or nearly pure He envelopes. Hot subdwarf stars play very important roles in the study of stellar evolution, especially for binary evolution. Furthermore, these stars are considered as the main sources of the ultraviolet (UV) upturn phenomena found in elliptical galaxies (O’Connell 1999; Han et al. 2007; Jenkins 2013). Due to the diversity of H and He abundances in the atmosphere of hot subdwarf stars, they are ideal objects to test chemical diffusion theory as well (Michaud et al. 2008, 2011).

Most sdB stars are considered to be formed in binary systems, since about half of these stars are found in close binaries (Maxted et al. 2001; Napiwotzki et al. 2004; Copperwheat et al. 2011). Employing a detailed binary population synthesis, Han et al. (2002, 2003) found that mass transfer through Roche lobe overflow (RLOF), common envelope (CE) ejection and merger of two He white dwarfs (WDs) can form sdB stars in binaries (also see Chen et al. 2013 and Xiong et al. 2017 for further study). Zhang et al. (2012, 2017) found that the merger of two He WDs or a He WD and a low-mass main-sequence (MS) star could produce single hot subdwarf stars, while Lei et al. (2015, 2016) demonstrated that tidally enhanced stellar wind in wide binaries is a viable formation channel for blue hook stars in massive globular clusters, which are the counterparts of field hot subdwarf stars.

Corresponding author: Gang Zhao
gzhao@nao.cas.cn

Corresponding author: Zhenxin Lei
zxlei@nao.cas.cn

arXiv:1810.09625v2 [astro-ph.SR] 29 Jun 2019

The number of known hot subdwarf stars remained at a low level until the Palomar-Green survey (PG, Green et al. 1986) of the northern Galactic hemisphere was released. With publicly available large surveys, such as Sloan Digital Sky survey (SDSS, York et al. 2000) and Large Sky Area Multi-Object Fibre Spectroscopic Telescope (LAMOST) survey (Cui et al. 2012; Zhao et al. 2006, 2012), etc, the number of known hot subdwarf stars increased largely in recent years. Geier et al. (2017) compiled a catalogue of known hot subdwarf stars from the literature and unpublished databases, in which more than 5000 hot subdwarf stars and candidates are listed.

The method of candidate selection is a very important step to identify hot subdwarf stars in large surveys. The conventional method is to use color cuts followed by visual inspections. Employing this method, Geier et al. (2011) identified more than 1100 hot subdwarf stars from the SDSS survey; Vennes et al. (2011) and Németh et al. (2012) identified more than 200 hot subdwarf stars in Galaxy Evolution Explorer (GALEX) survey, while Luo et al. (2016) found more than 100 hot subdwarf stars in the LAMOST survey. In contrast to these studies, Bu et al. (2017) employed a machine learning method to search for hot subdwarf stars in LAMOST DR1.

Fortunately, the selection of hot subdwarf candidates has become much easier recently thanks to the second data release (DR2) of Gaia (Gaia collaboration et al. 2018a). The data of Gaia DR2 provide us the accurate positions, parallaxes and photometry for a large number of objects in our Galaxy. With these information, one can build a Hertzsprung-Russell (HR) diagram for a huge number of stars, in which nearly all stellar evolution sequences are presented clearly, including the hot subdwarf sequences. In this paper, we selected more than 4000 hot subdwarf candidates from the Gaia DR2 HR diagram built by Gaia collaboration et al. (2018b). Combining with spectra from LAMOST DR5, we finally identified nearly 300 hot subdwarf stars from these candidates, among which 110 are newly identified in this study. To confirm the identifications further, we obtained the atmospheric parameters of these hot subdwarf stars by fitting the profiles of H and He lines with synthetic spectra. The structure of this paper is as follows: In Section 2, we describe the hot subdwarf candidate selection procedure from the Gaia HR diagram and the spectral analysis. We give our results in Section 3. Finally, a discussion and summary are given in Section 4.

2. TARGET SELECTION AND SPECTRAL ANALYSIS

2.1. *Gaia DR2 database and HR diagram*

Gaia DR2 was released on 25 April 2018 by the Gaia collaboration. Gaia DR2 consists of astrometric, photometric and radial velocity data, as well as variability and astrophysical parameters for objects brighter than 21^m (Gaia Collaboration et al. 2018a). It contains approximately 1.7 billion sources with apparent magnitudes in white-light G-band (330-1050 nm), among which for about 1.3 billion sources are given positions, parallaxes, proper motions as well as photometry in the Blue (BP, 330-680 nm) and Red (RP, 630-1050 nm) band.

With the accurate parallaxes and photometry provided by Gaia DR2, one can build a HR diagram for a huge number of stars. Gaia collaboration et al. (2018b) built the Gaia HR diagram by selecting sources with the most precise parallaxes and photometry from Gaia DR2. To remove most of the artefacts (Arenou et al. 2018) while reserve plenty of genuine binaries between the white dwarf (WD) sequence and the main-sequence (MS) in the HR diagram, Arenou et al. (2018) filtered out the astrometric excess noise by adopting the filter proposed in Appendix C of Lindergren et al. (2018). Gaia collaboration et al. (2018b) estimated the absolute magnitude using $M_G = G + 5 + 5\log_{10}(\varpi/1000)$, with ϖ the parallax in milliarcseconds. To ensure the validity of this equation, the relative uncertainty of the parallax is limited to be lower than 10%. Furthermore, filters for the relative flux errors on the G, G_{BP} and G_{RP} magnitudes are also applied, which remove variable stars from the HR diagram. The detailed selection filter are presented in Section 2 of Gaia collaboration et al. (2018b).

Panel (a) of Fig 1 shows the Gaia HR diagram, which contains 65 921 112 stars. Due to the effects of extinction, most of the evolution sequences, such as the MS, red giant branch (RGB) and asymptotic giant branch (AGB) are indistinguishable, only the WD and hot subdwarf sequences show up clearly. However, one can see that there are still many stars in the region between the main hot subdwarf sequence (e.g., structure near $M_G \approx 5$ and $BP - RP \approx -0.02$ in Fig 1) and the wide MS. These objects could be real hot subdwarf stars, binaries or artefacts suffering from serious extinction issues (Arenou et al. 2018). To maximize the number of hot subdwarf stars in our study, we selected all the hot subdwarf candidates within the pink polygon. Although this pink polygon is determined visually, it consists of the Extreme Horizontal Branch (EHB), which is the main hot subdwarf sequence, and nearly all the objects between the EHB and MS. There are in total 4593 hot subdwarf candidates in the polygon, which are marked by blue dots in Fig 1. Panel (b) of Fig 1 is the zoomed region where our hot subdwarf candidates in the Gaia HR diagram were selected.

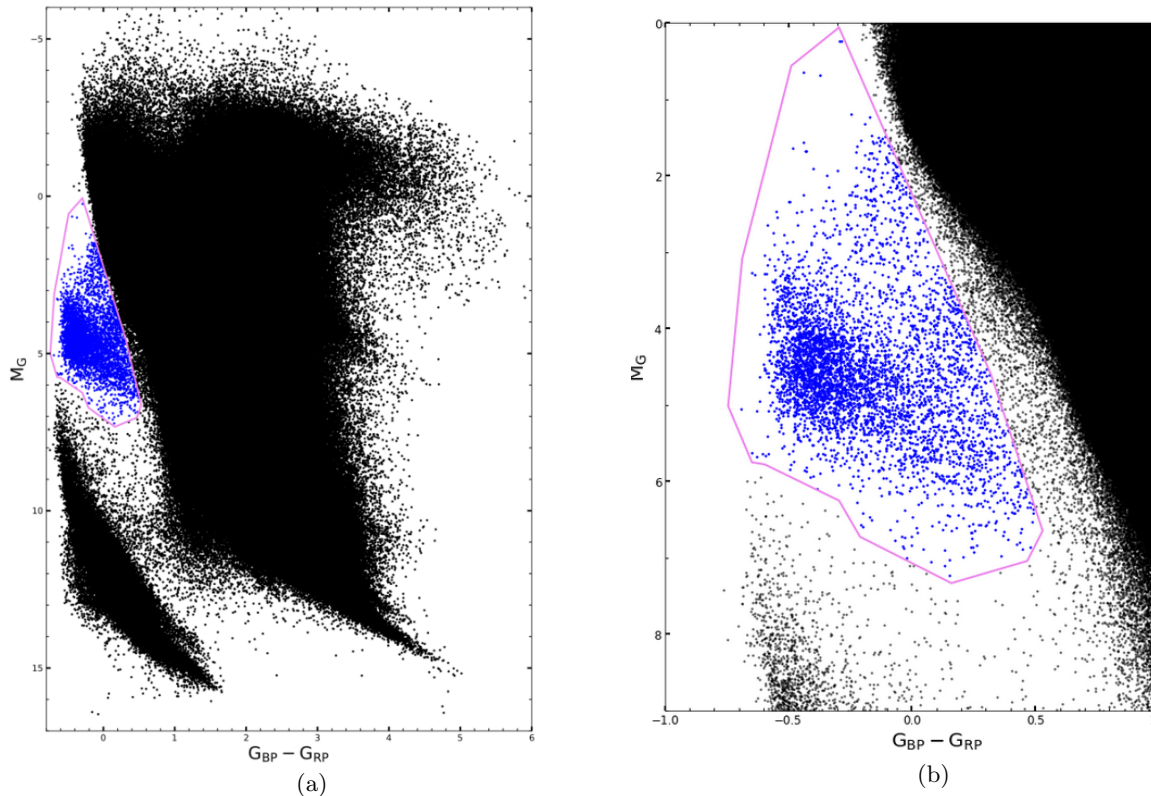


Figure 1. Panel (a): Gaia HR diagram from Gaia collaboration et al. (2018b). 4593 hot subdwarf candidates (blue dots) are selected visually within the boundaries of the hot subdwarf parameter space (pink polygon). Panel (b): Magnified drawing for the region of hot subdwarf candidates.

2.2. LAMOST DR5

LAMOST is a Chinese national scientific research facility operated by the National Astronomical Observatories, Chinese Academy of Sciences. It has a specially designed reflecting Schmidt telescope with 4000 fibers in a field of view of 20 deg^2 in the sky. By July 2017, LAMOST has completed its pilot survey and completed its first five years of regular survey which was initiated in September 2012. After this six-year-survey, LAMOST obtained 9 017 844 spectra in total with a resolution ($\lambda/\Delta\lambda$) of 1800 in the wavelength range 3690-9100Å, which consist of 8 171 443 stars, 153 090 galaxies, 51 133 quasars and 642 178 unknown objects. These data make up the fifth data release (DR5) of LAMOST.

We cross-matched our hot subdwarf candidates selected from the Gaia DR2 HR diagram with LAMOST DR5, and found 734 stars in common. To obtain reliable atmospheric parameters for these candidates, we removed the candidates with a signal to noise ratio (SNR) less than 10 from our sample. Moreover, we found that some candidates present obvious composite binary spectra, e.g., Mg I triplet lines at 5170 Å and/or Ca II triplet lines at 8650 Å, and some of them present obvious H Balmer emission lines. These spectra have been removed from our sample as well. Such composite spectra will be analyzed in a forthcoming paper with appropriate models. After these procedures, we obtained 490 hot subdwarf candidates suitable for spectral analysis.

2.3. Fitting LAMOST spectra with synthetic spectra

Non-LTE model atmospheres with TLUSTY (version 204; Hubeny & Lanz 2017) and synthetic spectra with SYNSPEC (version 49; Lanz et al. 2007) have been computed by Németh et al. (2014), which were adopted in our study to fit the H and He profiles of our sample spectra. The spectral fitting was carried out by XTGRID. This iterative procedure fits the observed spectrum by applying successive adjustments to the synthetic spectrum following the gradient of steepest descent in the χ^2 space (see Németh et al. 2012 for details). The synthetic spectra have been convolved with a Gaussian profile to match the resolution of the observed spectra, and the parameter errors were estimated by mapping the $\Delta\chi^2$ field until the 60 per cent confidence level at the given number of free parameters was reached.

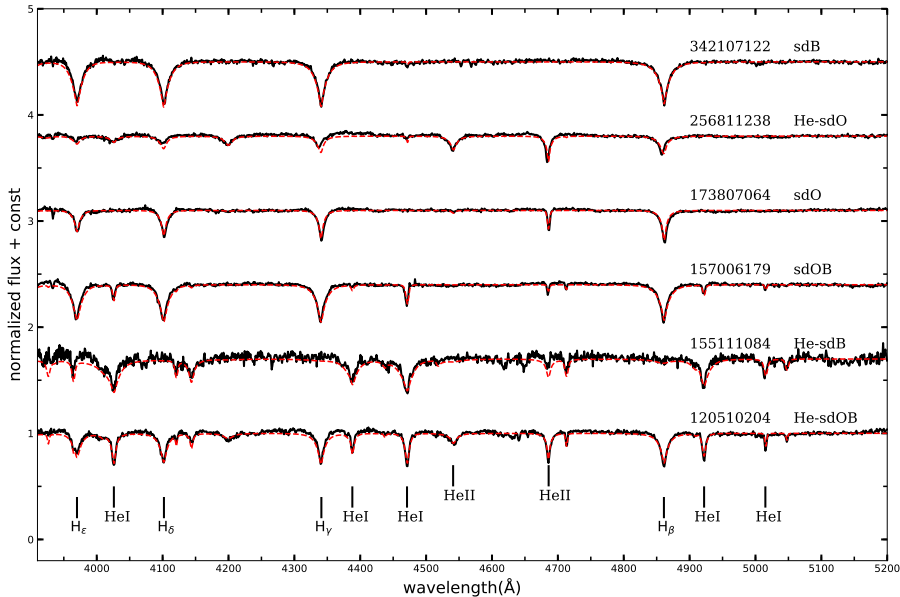


Figure 2. Normalized spectra for some hot subdwarf stars identified in this study. Black solid curves are normalized observed spectra, and the red dashed curves are the best-fitting synthetic spectra. Some important H and He lines are marked by short vertical lines at the bottom of the figure. The LAMOST_obsid and spectral classification type are presented on the right side for each spectra.

Fig 2 shows examples of fitting results in our study. In this figure, black solid curves are the normalized spectra for our candidates, while red dashed curves are the best-fitting synthetic spectra found by XTGRID. Some important H and He lines are presented by short vertical lines at the bottom of Fig 2 as well. Furthermore, the LAMOST_obsid and spectral classification type for each star are also given in the right side of Fig 2. We followed the classification scheme of Geier et al. (2017, see their Table 1) to classify our hot subdwarf stars.

The top spectrum in Fig 2 (i.e., 342107122) presents dominant H Balmer lines but no He lines, which is a typical sdB star. The second spectrum from the top (i.e., 256811238) is a typical He-sdO star, because it shows dominant He II lines but very weak H Balmer and He I lines. The third spectrum from the top (i.e., 173807064) is classified as a sdO star, since it presents strong H balmer lines with weak He II line at 4686 Å, but no He I lines are detected. On the other hand, the fourth spectrum from the top (i.e., 157006179) is classified as a sdOB star, because it presents strong H Balmer lines combined with both weak He I and He II lines. The fifth spectrum from the top (i.e., 155111084) shows dominant He I lines but no H Balmer and He II lines, which is typical to He-sdB stars based on the classification scheme of Geier et al. (2017), while the bottom spectrum (i.e., 120510204) shows dominant He I lines but also with He II and H Balmer lines, therefore we classified it as a He-sdOB star.

3. RESULTS

By fitting the observed spectra with synthetic spectra, we obtained the atmospheric parameters (e.g., T_{eff} , $\log g$, $\log(n\text{He}/n\text{H})$) for the entire sample. Candidates with $T_{\text{eff}} < 20\,000$ K and $\log g < 5.0$ were considered as BHB stars, while candidates with $\log g < 4.5$ were considered as B type MS stars (Németh et al. 2012). By removing BHB, B type MS stars and duplicate objects, we identified 294 hot subdwarf stars, which include 169 sdB, 63 sdO, 31 He-sdOB, 22 sdO, 7 He-sdO and 2 He-sdB stars.

All the parameters for our identified hot subdwarf stars are presented in Table 1. Columns 1-4 give the right ascension (RA), declination (Dec), LAMOST_obsid and Gaia source_id. Next, columns 5-8 give the T_{eff} , $\log g$, $\log(n\text{He}/n\text{H})$ and radial velocity (RV) fitted by XTGRID. Columns 9-11 list the apparent magnitude in the Gaia G band, the SNR in the u band and the spectral classification type, respectively. We cross-matched our results with the latest hot subdwarf catalogue of Geier et al. (2017), and got 184 common stars. We also cross-matched our results with the hot subdwarf stars identified in Németh et al. (2012) and Luo et al. (2016), and obtained 29 and 35 common stars, respectively. The objects marked with * in Table 1 are common hot subdwarf stars listed in the catalogue of Geier et al. (2017), while objects labeled with † and ‡ are common with Németh et al. (2012) and Luo et al. (2016) respectively. '>' in

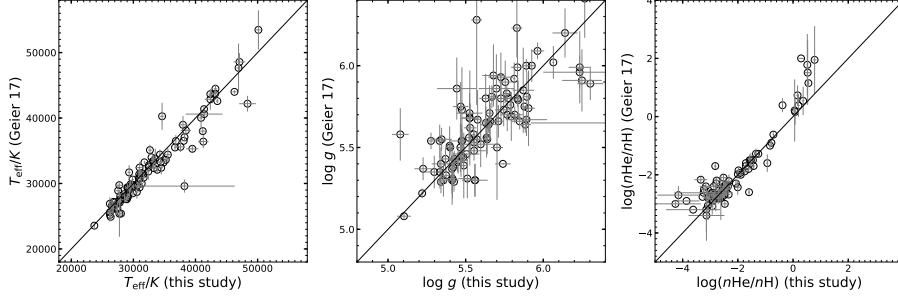


Figure 3. Comparisons of atmospheric parameters between this study and Geier et al. (2017).

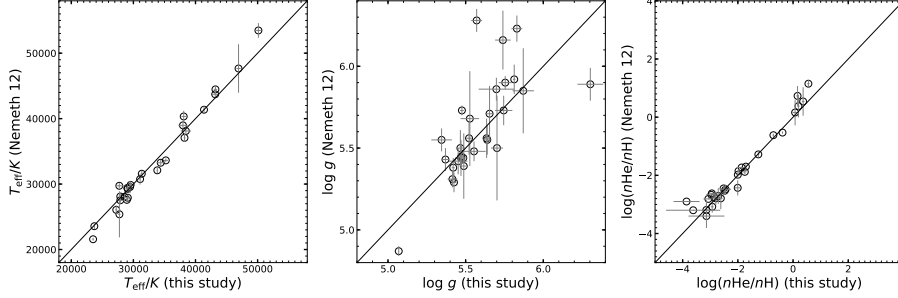


Figure 4. Comparisons of atmospheric parameters between this study and Németh et al. (2012).

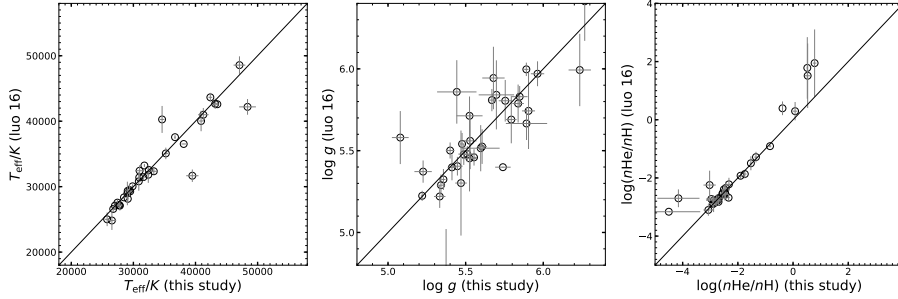


Figure 5. Comparisons of atmospheric parameters between this study and Luo et al. (2016).

$\log(n\text{He}/n\text{H})$ denotes an upper limit of the He abundance, when XTGRID could not find the error bars at the given quality of the spectra.

3.1. Comparison with other studies

Fig 3 shows the comparison of atmospheric parameters for the common stars between this study and Geier et al. (2017), for which atmospheric parameters are available. One can see that both T_{eff} (left panel) and $\log(n\text{He}/n\text{H})$ (right panel) agree well. Although the comparison of $\log g$ (middle panel) presents a little larger dispersion than the other two parameters, our results are comparable with the values from Geier et al. (2017). Fig 4 and Fig 5 show the comparison between the results from our study and the results by Németh et al. (2012) and Luo et al. (2016), respectively. Similarly, the values of T_{eff} (left panel) and $\log(n\text{He}/n\text{H})$ (right panel) obtained in our study are very similar to the values obtained in Németh et al. (2012) and Luo et al. (2016) for the same stars. The value of $\log g$ (middle panel) are also comparable between these studies. Note that the atmospheric parameters in Németh et al. (2012) are obtained by employing XTGRID as well. The synthetic spectra in Németh et al. (2012) are calculated from atmospheric models not only with H and He compositions, but also with C, N, O compositions, while the synthetic spectra in our study and Luo et al. (2016) are calculated from atmospheric models with only H and He composition (Németh et al. 2014). A comparison of Fig 4 and Fig 5 reveals that at the given resolution and SNR the composition has only a little influence on our final results.

Table 1. The information of 294 hot subdwarf stars identified in this study. From left to right, it gives the right ascension (ra), declination (dec), LAMOST_obsid, and Gaia source_id. Next the T_{eff} , $\log g$, $\log(n\text{He}/n\text{H})$ and radial velocity (RV) are listed from the XTGRID fits. Next, the apparent magnitudes in the Gaia G band, the SNR for the u band and the spectral classification types are listed, respectively.

ra ^a	dec ^b	obsid ^c	source_id	T_{eff}	$\log g$	$\log(n\text{He}/n\text{H})^d$	RV	SNRU	G	spclass
LAMOST	LAMOST	LAMOST	Gaia	(K)	(cm s^{-2})		km s^{-1}		Gaia(mag)	
0.0767*	22.30079	385816105	2847977322031768832	28810±280	5.57±0.03	-2.68±0.10	103.3	38.69	14.24	sdB
0.278039*	11.010084	66605009†	2765454164004531328	27030±210	5.48±0.02	-2.70±0.06	-35.6	21.58	13.61	sdB
0.981681*	27.810404	492112073	2854091981071865344	28000±90	5.56±0.02	-2.76±0.04	147.4	85.58	13.33	sdB
3.580483*	22.40487	487408198	2800515322070491008	36160±810	5.35±0.07	-3.12±0.34	7.8	12.21	13.43	sdB
8.943925*	26.915094	157510209	2809421366255514112	27150±520	5.58±0.06	-2.44±0.09	32.8	35.58	14.28	sdB
9.166037*	37.931859†	75913167	368263110278860544	37980±750	6.30±0.08	-3.00>	213.2	15.23	14.14	sdB
9.507177	34.53228	14610118	365002268028633600	40620±280	5.55±0.07	-0.27±0.07	73.6	15.63	13.90	He-sdOB
11.70128*	19.93683	285308094	2801277176253968640	32230±250	5.89±0.06	-2.27±0.06	18.6	39.38	14.98	sdB
11.918803*	31.398766	186304225	360511037906831872	30990±280	5.75±0.04	-2.24±0.05	81.0	45.85	14.81	sdB
12.321444*	20.944565†	164803013	2801448085887897216	27890±580	5.34±0.07	-2.44±0.20	6.2	20.10	14.56	sdB
12.455266*	35.366938	14604029	363795760175504768	35150±440	5.78±0.06	-1.54±0.06	11.9	29.80	14.82	sdOB
13.640353*	37.970977	82010071	364742852004132736	33680±530	6.08±0.09	-1.87±0.10	87.7	19.91	14.62	sdOB
14.602768*	1.909744	8206211‡	2537690089791382656	33290±600	5.53±0.08	-1.90±0.10	-53.7	22.52	15.13	sdOB
15.305503*	31.432091	96302063	312628749626419328	27150±250	5.48±0.02	-2.89±0.10	-41.9	50.74	13.08	sdB
16.090314*	4.226959	55112148‡	2551900379931546240	27760±180	5.55±0.02	-2.72±0.05	30.3	31.77	12.05	sdB
16.203409*	36.461784	82001006	369576820516013824	32270±70	5.77±0.02	-1.64±0.02	10.7	113.49	12.40	sdOB
17.44054*	37.760636	23008132	369573831218501376	29070±160	5.49±0.03	-3.44±0.43	33.8	13.43	13.87	sdB
19.870333*	49.019264†	82712038‡	400211958948711552	43170±520	5.70±0.11	0.07±0.09	-1.4	11.41	13.37	He-sdOB
21.65453*	16.1365	363615074	2592234628262141312	30490±130	5.72±0.01	-2.42±0.03	33.8	96.43	14.31	sdB
23.849927*	37.34115	401302195	322575344128842624	55470±950	5.33±0.26	0.55±0.13	26.6	98.86	14.11	He-sdO
24.109146*	11.658952	482304144	2585744516065582848	29590±510	5.71±0.02	-2.26±0.05	43.9	32.60	12.30	sdB
27.72618	31.129651	14713190	304311150320629376	28520±270	5.74±0.03	-1.73±0.05	76.3	17.08	14.32	sdB
28.324146	35.701356	354713006	330261789400007040	29860±430	6.06±0.08	-2.67±0.23	-39.9	10.37	15.73	sdB
28.591037*	49.089103†	503213129	357580873780641920	33850±100	5.70±0.04	-2.00±0.07	83.8	12.42	13.47	sdB
29.647084	55.084686	380703127	504485110543295616	51300±3500	5.24±0.04	-2.31±0.12	21.1	47.42	15.52	sdO
30.5077	56.7284	15302097	505063728541561344	28920±590	5.62±0.07	-2.47±0.11	-39.2	12.48	15.24	sdB
31.537384*	37.647643	510514015	330722897089067392	27630±220	5.41±0.03	-2.85±0.12	32.0	28.37	14.17	sdB
33.110821*	1.921483	290113234	2514278566658235776	31650±370	5.63±0.02	-2.71±0.12	-41.1	30.45	14.19	sdB
33.708238*	23.331535	379610233	101096658200679936	26600±240	5.63±0.04	-3.16±0.23	34.6	35.94	15.67	sdB
34.42565	28.058199	173213178	107665724780053376	33120±110	5.92±0.04	-1.61±0.03	10.1	86.75	11.78	sdOB
38.216289*	44.190928†	180412223	341195058149873024	34400±570	5.75±0.06	-1.71±0.04	-60.2	36.48	14.27	sdOB
38.317737	8.380032	364610005	20063858119453824	29830±110	5.43±0.03	-2.39±0.07	31.2	17.22	15.38	sdB
40.844775*	4.843528	293409213	6052403489630720	34790±110	6.02±0.03	0.09±0.03	-64.8	103.08	14.09	He-sdOB
41.89582*	36.763992	82312150‡	141428363911552384	43520±210	5.89±0.13	0.52±0.03	74.4	48.24	12.98	He-sdOB
45.315923*	-2.670405	367406216	5186434732342771968	26820±230	5.39±0.02	-2.46±0.05	18.6	66.16	13.84	sdB
49.487181	32.497341	76704053	125093503772825856	34250±230	5.97±0.05	-1.62±0.05	74.7	15.51	15.72	sdOB
50.662367*	46.076037	408714065	242734753958329728	41490±50	5.76±0.06	1.19±0.09	69.8	15.61	13.66	He-sdOB
50.989343	42.270805	353410213	240978868246214400	35350±440	5.81±0.08	-1.45±0.07	14.8	17.34	15.77	sdOB
51.907159*	38.135982	265511138	234861632224434324	26010±150	5.52±0.01	-2.84±0.05	-104.5	62.88	14.22	sdB
53.288922	34.208582	292911128	221005208733887488	34540±420	5.64±0.05	-1.67±0.04	26.4	21.33	15.79	sdOB
54.589981	41.734607	296711237	237331822538478592	27200±140	5.59±0.03	-1.51±0.03	9.1	30.37	15.21	sdB
54.696112	41.573393	296715043	237133566847520000	22240±320	5.76±0.03	-3.00>	100.8	30.84	15.11	sdB
54.944312	35.546154	265506073	221375331836119552	64650±9600	5.61±0.05	-1.58±0.08	23.0	26.89	15.84	sdO
56.022214	22.072953	249811209	64368713521485568	28130±440	5.59±0.06	-2.74±0.09	29.7	32.31	14.40	sdB
57.933712	36.871319	181511115	220091342774317056	28170±320	5.37±0.08	-2.58±0.43	31.8	10.59	16.18	sdB
58.380531*	10.751119	159408059	3303143628052101120	42400±230	5.70±0.05	-0.01±0.06	-30.5	62.97	12.83	He-sdOB
58.809479*	10.470014	159306197	330295130527310464	26340±150	5.33±0.01	-2.68±0.06	35.0	16.40	14.15	sdB
59.276419	36.474847	397401216	220172981513287936	84550±3640	5.58±0.04	-1.30±0.15	25.6	22.98	15.49	sdO
60.052436	36.596069	397401025	219511728348315520	22480±120	5.36±0.02	-3.07±0.22	18.3	20.86	14.89	sdB
60.197058	17.311691	280513233	46608061680943872	28750±290	5.57±0.04	-3.15±0.20	23.7	17.22	15.45	sdB
60.675411	31.397095	182113038	169258102724229888	36410±340	6.00±0.10	-1.52±0.08	-48.6	13.70	15.83	sdOB
61.093981	37.408948	397507109	225573267233289600	34470±290	5.72±0.10	-1.43±0.09	8.5	19.94	16.20	sdOB
63.958993*	1.905817	174708071	3259060049366022400	32920±90	5.78±0.02	-1.71±0.03	9.8	87.29	14.04	sdOB
64.820704	36.473358	162001168	177389712764641920	42340±250	5.47±0.05	-0.38±0.04	-7.8	39.03	14.62	He-sdOB
65.998459	34.463668	204704027	176209799348981376	35580±220	5.79±0.04	-1.49±0.04	82.6	41.01	15.19	sdOB
66.040252	8.554802	425604162	3299455110137611776	27210±190	5.27±0.01	-1.32±0.02	-0.5	142.89	12.53	sdB
67.389212*	7.697824	527312249	328714463435536768	44080±1010	5.62±0.04	-2.40±0.08	18.2	34.29	15.07	sdO
67.80107*	42.986157	420301136	252329740960393984	26690±180	5.63±0.01	-2.71±0.06	32.8	63.34	14.56	sdB
71.237089*	14.363909	282807077	3308791681845675136	32660±320	5.66±0.05	-2.49±0.13	-54.0	16.33	14.97	sdB
71.814516*	20.666174	283416013	3411847601045302144	30250±700	5.51±0.12	-1.88±0.24	29.2	13.79	15.55	sdB
72.196713	-4.00472	392308023	3200857538788110080	29370±50	5.65±0.01	-1.97±0.03	17.9	44.84	13.36	sdB
73.990376	46.318864	364911218	254631847728048384	27250±430	5.45±0.04	-2.73±0.23	-108.9	14.90	15.72	sdB
75.660378	45.720627	364912013	206657161813612288	32840±210	6.04±0.05	-1.92±0.07	-52.1	13.61	15.67	sdB
76.68493	11.604413	407202008	3388118112893920000	32480±210	5.34±0.12	-1.31±0.06	72.3	26.66	15.42	sdOB
77.306642	33.503376	209916235	181774221540061824	25640±200	5.32±0.01	-2.13±0.05	-59.6	21.09	15.44	sdB
77.51154*	12.879591	407205159	3388371103647349632	32300±160	6.06±0.05	-2.09±0.07	7.8	12.46	16.07	sdB
77.963858*	41.691511	252814174	201146826149598464	31530±350	6.26±0.15	-2.56±0.23	-21.3	12.06	15.58	sdB
78.457499*	17.706998	317806011	3395250473024213120	30990±200	5.50±0.05	-1.97±0.04	11.0	11.26	14.06	sdB
80.378419	37.362848	162512222	184468780942344960	26600±300	5.72±0.05	-3.00>	108.7	11.86	14.28	sdB
80.96406	14.078763	374402025	3390235531771243904	21770±120	5.01±0.05	-2.17±0.06	31.4	30.53	15.86	sdB

^aStars labeled with * also appear in the hot subdwarf catalogue of Geier et al. (2017).

^bStars labeled with † also appear in Németh et al. (2012).

^cStars labeled with ‡ also appear in Luo et al. (2016).

^d">" denotes an upper limit of $\log(n\text{He}/n\text{H})$ for the object.

Table 1. continued.

ra ^a	dec ^b	obsid ^c	source_id	T_{eff}	log g	log(nHe/nH) ^d	RV	SNRU	G	spclass
LAMOST	LAMOST	LAMOST	Gaia	(K)	(cm s^{-2})		km s^{-1}		Gaia(mag)	
83.279828	7.506107	208913243	3334223901191558784	35370±1050	5.89±0.06	-1.66±0.07	-57.1	33.66	13.81	sdOB
83.338169	16.113207	258002165	3396876131029433472	33930±290	5.92±0.05	-1.66±0.05	80.1	28.37	15.23	sdB
83.465224	19.241956	279007127	3400946935393688576	27170±250	5.36±0.03	-3.03±0.19	-34.2	17.48	15.76	sdB
84.235335*	39.92188	42704127	190970433715259904	37890±330	5.57±0.06	-0.63±0.06	-0.5	17.17	13.92	He-sdOB
85.740707	39.197564	284213200	190164354254168192	36580±400	5.68±0.06	-1.49±0.06	17.6	11.36	14.94	sdOB
86.189735	30.648213	408809093	3444598749605672064	28520±150	5.59±0.02	-2.50±0.04	33.9	41.89	12.43	sdB
86.235913	35.826651	319909136	3455626713794023680	45570±180	5.60±0.04	0.47±0.05	-0.4	37.80	15.26	He-sdOB
86.775955	40.139606	321102181	191727718051389312	32880±300	5.88±0.05	-1.24±0.05	6.6	21.52	15.76	sdOB
87.96384	22.076954	107916117	3424202297812639360	29210±190	5.60±0.02	-2.22±0.04	13.7	24.41	13.17	sdB
88.167219*	19.820386	195804131	3398928751737464192	80890±14680	5.58±0.11	-2.21±0.28	-29.2	28.36	14.86	sdO
88.302057*	19.397253	195805160	3398852881140229632	29140±190	5.56±0.02	-2.80±0.16	-40.2	38.34	14.53	sdB
88.453581	32.93382	66503084	3451217092350738944	30500±80	5.66±0.02	-2.18±0.03	-51.8	50.97	14.17	sdB
89.391565	14.204803	271101097	3346893264443563776	37240±290	5.59±0.03	-1.43±0.04	-52.9	33.36	14.55	sdOB
89.707524	18.519722	195807009	3350560685476251648	29880±370	5.40±0.08	-2.60±0.22	-35.5	19.27	15.65	sdB
90.129088	29.148612	212009005	3431631727942970240	35000±140	5.34±0.03	-0.87±0.03	-64.1	39.35	13.19	He-sdOB
90.157054	36.799292	381508201	3456632255835216640	26300±1160	5.30±0.14	-3.24±0.29	-33.8	13.38	15.46	sdB
90.257966	42.511474	321109600	960904069540367232	35770±270	5.90±0.05	-1.51±0.04	14.8	30.16	15.28	sdOB
91.22292	9.467549	526403092	3329611552994806272	47960±640	5.70±0.11	0.17±0.05	-104.4	20.84	14.56	He-sdO
92.665509	7.903821	526401140	3328247780618525568	27850±370	5.47±0.03	-2.76±0.11	-40.0	25.65	15.06	sdB
92.742942	13.375245	400104005	3344349578650746880	29070±320	5.61±0.09	-3.00>	-16.9	18.48	16.02	sdB
92.845855	55.870869	497610101	997207297787944064	29780±470	5.46±0.07	-2.46±0.13	9.5	25.00	15.81	sdB
93.304375*	34.933493	187212172	3452480293768439296	28970±280	5.49±0.07	-3.00>	-35.5	27.35	14.47	sdB
93.636538	11.061654	398805096	3330105641733251840	31300±220	5.47±0.04	-1.83±0.06	12.0	13.18	16.41	sdOB
94.475909	23.631485	176413170	3425561981379261184	31620±470	5.70±0.07	-1.52±0.02	7.5	18.12	15.39	sdOB
94.486139	18.83019	555306021	3373814561832902272	26600±480	5.47±0.05	-2.91±0.15	-39.9	24.90	13.60	sdB
94.678473*	21.592955	483207093	3376639486380091008	31380±60	5.80±0.02	-2.95±0.08	-35.2	59.50	14.67	sdB
94.864687*	35.382661	220504054	3452740362628172160	35590±210	5.53±0.02	-3.00>	-58.4	55.90	15.05	sdOB
95.205672	19.308045	256512020	3373940219694568576	30420±100	5.71±0.02	-2.05±0.07	-54.4	16.85	14.96	sdB
96.592792	4.073252	442708048	3131204469305148288	26620±70	5.53±0.01	-2.78±0.05	23.6	68.24	12.32	sdB
96.770481*	34.969325	74716039	9424634341784405076	25330±540	5.30±0.05	-3.34±0.30	29.6	12.20	14.43	sdB
97.152155	32.842084	74703090	3439296187280018432	43240±610	5.49±0.09	0.11±0.07	-5.9	23.47	14.71	He-sdOB
97.640728	21.324502	274309125	3376057123175008256	21460±240	5.32±0.02	-2.36±0.20	-38.6	15.27	15.33	sdB
98.043207	28.178276	75709065	3434099173772378112	45110±610	5.44±0.08	0.40±0.07	-0.7	18.17	15.10	He-sdOB
98.497308	32.553966	74704076	3436238720320660224	26010±1210	5.86±0.11	-2.97±0.42	-57.6	13.01	15.16	sdB
99.967315	51.950267	117705238	992534888766785024	26230±240	5.97±0.01	-2.99±0.13	-103.2	40.08	11.96	sdB
100.45235*	45.805621	422811236	963881581386403072	28140±320	5.56±0.06	-2.77±0.14	-100.8	28.19	14.20	sdB
100.81184	13.965445	415715194	3352890447538648064	32560±260	5.76±0.04	-2.18±0.05	-51.5	24.60	14.90	sdB
100.88299*	14.157207	415715176	3355897092143865088	35930±180	5.57±0.02	-3.00>	-54.3	27.31	14.83	sdB
100.948932*	32.029482	438514106	937248901501446272	26880±70	5.21±0.01	-2.70±0.05	-37.5	29.84	13.83	sdB
101.57652*	29.337016	2604051	3386622158606040960	37930±360	6.00±0.05	-3.00>	-101.5	74.81	13.59	sdB
103.09651	9.965476	392002223	3158419684195782656	70180±1800	5.78±0.04	-1.44±0.10	-44.4	88.90	14.22	sdO
103.18157	40.293805	296115026	950627174872167808	68730±1180	5.21±0.03	-0.29±0.05	96.3	92.62	14.13	He-sdO
103.351374	33.059526	438511176	937556831431448192	33990±100	5.49±0.01	-1.49±0.03	-268.2	107.46	12.11	sdOB
103.69431	24.82412	81505213	3381286602335612416	61260±2250	5.10±0.02	-2.00±0.07	-40.6	55.28	13.99	sdO
103.88743	22.063784	95406046	3378454092881858816	32780±940	5.69±0.06	-1.70±0.08	-50.3	32.78	13.70	sdOB
104.56965	9.728642	29001011	3157967411257049728	36690±1110	5.01±0.07	-1.74±0.05	-53.1	18.19	13.59	sdOB
106.31091	22.355964	174911065	3367827072481260416	28550±280	5.62±0.04	-2.71±0.12	-36.8	28.70	15.12	sdB
106.82751	14.016182	372807096	3161497015379649280	39820±1010	5.61±0.07	-1.95±0.14	8.2	32.01	15.42	sdOB
108.01	11.559014	128701029	3159937564294110080	25790±160	5.43±0.01	-2.65±0.04	28.7	48.56	12.46	sdB
108.62448*	22.283159	177904103	3367249485278272000	41840±10	6.10±0.06	0.76±0.04	-19.3	257.09	11.61	He-sdOB
109.740975*	2.887462	492402100	3139042514040855296	26300±160	5.23±0.02	-2.46±0.10	-34.5	16.45	14.89	sdB
110.666731	9.231818	369611044	3155626997678101248	48010±2010	5.79±0.09	-2.71±0.29	18.7	22.22	13.05	sdO
110.96446*	30.321259	214908131†	885963418573729792	32400±190	5.91±0.04	-1.53±0.04	17.5	44.35	15.04	sdOB
111.22127*	19.391139	270103045	3362730178953977472	26520±120	5.53±0.02	-2.54±0.05	-56.0	53.35	14.67	sdB
111.22289	15.280799	397603157	3167124522048560128	32490±400	5.88±0.08	-1.77±0.08	-63.2	39.25	15.54	sdOB
111.65522	8.558556	446301096	3143342600936696960	29920±130	5.64±0.02	-3.00>	-158.5	50.05	15.03	sdB
113.35669*	36.882668	331004092	898625493262383104	33110±80	5.94±0.02	-2.42±0.04	-39.4	58.95	15.10	sdB
114.182985	-3.195907	436206051	3060798513530161920	28890±400	5.54±0.04	-1.11±0.04	-65.6	32.14	13.75	sdB
114.48439	31.279597	91905056	880252005422941440	31000±290	5.49±0.05	-2.42±0.09	12.0	10.95	13.58	sdB
114.51894*	26.412458†	73906248	869050009160765056	27730±660	5.55±0.07	-3.14±0.65	-99.8	10.74	14.58	sdB
116.14643*	30.352421†	120407017	879166065892619904	29100±350	5.45±0.06	-2.86±0.10	32.5	36.33	14.74	sdB
116.28351*	38.18521	279210190	919963474904219776	29310±270	5.30±0.06	-0.93±0.04	1.0	40.58	14.84	sdB
116.46916	25.85761	183702062	868817943488022016	26210±250	5.47±0.03	-2.31±0.09	34.7	46.95	14.75	sdB
117.23262*	30.713059†	120407139	879237740307303040	31080±90	5.65±0.02	-1.98±0.04	-122.1	42.67	14.06	sdB
117.91362	6.768001	120510204	3144058245567712512	39600±80	5.61±0.07	-0.14±0.02	4.4	47.16	13.50	He-sdOB
118.55157*	29.832504	2711238	877431345781684480	31270±1010	5.82±0.19	-1.75±0.16	-42.3	15.02	14.57	sdB
119.01571*	22.441942†	173807064	674255203425267584	65800±1420	5.48±0.01	-2.00±0.10	-40.1	79.20	14.19	sdO
119.53142*	-4.534807†	170213155	3068507812327598208	41370±60	5.87±0.07	0.36±0.05	-98.2	54.63	13.06	He-sdOB
121.73617*	15.455543†	392709195†	654866823401111168	29030±240	5.47±0.04	-2.96±0.19	31.7	25.42	14.77	sdB
123.14029*	16.023232†	227309093	655674865665718656	31350±130	5.52±0.02	-3.00>	-94.2	52.05	13.69	sdB
126.89565*	17.898859†	268107224	662146419308286976	29460±200	5.64±0.03	-1.26±0.03	-110.8	47.66	14.58	sdB
127.136949*	14.867359†	380214234	651745279826458112	38230±150	5.81±0.01	-0.71±0.02	-19.3	167.39	11.64	He-sdOB
128.551254*	7.202881†	340409136	595824702553000448	29550±130	5.63±0.01	-2.94±0.11	-32.1	47.46	14.68	sdB
128.849472*	-1.931296	183405148	3073231760953563264	46270±330	5.88±0.04	0.29±0.10	4.5	127.86	11.38	He-sdOB
128.898243	19.736805	399207128	662848247026938240	27170±440	5.41±0.05	-2.65±0.11	-56.0	17.61	13.10	sdB

Table 1. continued.

ra ^a	dec ^b	obsid ^c	source_id	T_{eff}	$\log g$	$\log(n\text{He}/n\text{H})^{\text{d}}$	RV	SNRU	G	spclass
LAMOST	LAMOST	LAMOST	Gaia	(K)	(cm s^{-2})		km s^{-1}		Gaia(mag)	
130.432816*	13.075019 [†]	382027118	603097422215268736	46930±340	5.53±0.06	0.16±0.05	-34.7	92.85	13.61	He-sdOB
130.770989*	33.462441	199614008	710337051880367616	27360±530	5.47±0.03	-2.80±0.15	95.7	19.23	14.91	sdB
130.919521	2.007522	449410221	3078888851357039360	42780±1070	5.28±0.05	-2.82±0.16	22.5	34.53	14.03	sdO
131.39858	19.697389 [†]	535915112	661156102927711104	23510±90	5.07±0.00	-1.86±0.17	-41.1	66.89	13.26	sdB
133.348574*	16.826456	116809080 [‡]	611684298790301568	27820±210	5.41±0.03	-2.77±0.08	-38.1	18.30	13.93	sdB
134.205286*	17.020746 [†]	116812014 [‡]	611587919724027392	29080±420	5.49±0.02	-3.07±0.18	32.8	31.59	12.81	sdB
134.71299*	2.170267	109804103	577763368640517760	48090±1480	5.62±0.06	-1.93±0.14	-46.5	20.17	13.63	sdO
134.761016	11.94105	93916015 [‡]	604794342318395520	25770±360	5.61±0.03	-3.00>	-100.7	12.94	13.47	sdB
136.4204*	12.207931 [†]	531216109	604474251290699776	28570±110	5.47±0.03	-2.62±0.07	12.4	46.95	14.62	sdB
137.605977*	12.140855	94009080 [‡]	604238612204857088	27430±110	5.36±0.01	-2.82±0.05	22.2	30.75	13.93	sdB
138.03039*	16.222359	200801161 [‡]	607898538520616704	39490±990	5.37±0.04	-3.02±0.22	-49.2	89.45	13.81	sdO
138.215253*	27.342056	44602153 [‡]	695059062934110592	36700±120	5.96±0.04	-0.83±0.04	-14.5	48.12	12.21	He-sdOB
140.36756*	2.767307	101704108 [‡]	3845583703883921920	31610±240	5.84±0.04	-2.46±0.10	-50.4	26.27	13.30	sdB
140.665973*	27.040402	100508062 [‡]	694109462844643072	31770±70	5.89±0.01	-2.51±0.08	32.4	29.49	12.62	sdB
140.805888*	29.449328	29.449328	695726844449223040	30870±300	6.24±0.07	-1.34±0.06	-56.4	16.65	14.71	sdOB
142.233763*	6.276275 [†]	223707059	586043309672965888	27240±150	5.47±0.01	-2.80±0.07	30.4	36.65	14.10	sdB
142.564419*	30.842911	556014133 [‡]	697406932576439680	29100±160	5.67±0.02	-2.34±0.05	-113.8	48.05	14.88	sdB
142.74847*	2.842343	206408094	3844661557225496064	31340±210	5.58±0.02	-2.56±0.07	-55.4	29.48	14.95	sdB
144.543089*	-3.999546	408905050	3824642199263291136	34410±290	5.87±0.03	-1.82±0.06	-55.3	27.95	14.68	sdOB
146.299391*	-3.155844	408906081	3826259821385575296	40330±510	6.24±0.03	-3.00>	31.3	66.40	13.97	sdO
149.884416*	36.30718	90914031 [‡]	795959630108543232	27620±180	5.22±0.01	-2.70±0.30	32.4	65.43	12.82	sdB
150.976151*	40.571695	99507015 [‡]	803736166614876544	41260±850	5.33±0.04	-2.88±0.18	22.4	52.52	13.27	sdO
159.90309*	43.102566	228703057	781164326766404736	71950±5110	5.67±0.03	-1.74±0.04	30.3	98.07	11.11	sdO
162.511777*	-0.010237	205211114	3806303066866089216	34850±90	5.83±0.07	-1.89±0.06	13.6	49.68	13.43	sdOB
165.973167*	11.001214	290015051	3868458111291375616	35750±1050	5.87±0.34	-1.55±0.30	5.4	27.11	15.12	sdOB
169.205762	6.992267	401216228	3817717887347994112	30570±30	5.60±0.01	-2.52±0.05	16.3	45.34	13.00	sdB
170.001536*	30.950015	300414223	4023386553845346688	33620±350	5.77±0.04	-2.33±0.08	10.8	34.28	14.51	sdOB
170.961175*	23.612733	309515234	3992841536709888640	28080±60	5.38±0.01	-2.36±0.03	-37.6	67.31	14.15	sdB
172.51545*	1.627016	237307119 [‡]	3799987433421443712	42390±300	5.68±0.07	0.78±0.07	-23.0	36.42	13.79	He-sdOB
181.601508*	57.159922 [†]	25714089 [‡]	1575432697534110336	35220±350	5.75±0.04	-1.75±0.06	80.6	26.21	14.85	sdOB
188.963098*	42.377703	133410210 [‡]	1534536701840624768	26750±220	5.51±0.06	-2.56±0.07	-38.5	30.67	11.99	sdB
189.219429*	50.253856	22713239 [†]	1568451554613413888	48380±1350	5.23±0.06	-2.32±0.12	92.6	21.98	14.65	sdO
189.347983*	25.06663	555614008	395963123467004704	33220±370	6.14±0.08	-1.61±0.11	6.5	12.28	10.47	sdOB
190.159493*	51.266733	455403016	156856988952108800	42190±180	5.72±0.05	0.69±0.01	64.9	77.38	13.58	He-sdOB
190.629575*	4.112153	206508081	3704162319296853120	34180±60	5.87±0.02	-2.04±0.03	-49.2	28.42	15.48	sdOB
192.709449*	16.167535	100802163 [‡]	3934486949931442176	26540±690	5.53±0.05	-2.47±0.10	-37.1	18.93	14.41	sdB
194.455489*	54.42649	415303223	1570270249924113408	33130±150	5.89±0.02	-1.55±0.04	4.3	49.83	13.50	sdOB
194.838437*	27.568081	301804130	1460692714941449728	35550±590	5.73±0.08	-0.79±0.07	-65.6	12.95	14.19	He-sdOB
195.67403*	27.678316	235908240	1460730407575030656	38220±8090	6.74±0.82	-2.07	407.3	10.97	14.21	sdB
196.516153*	9.408616	342107122	3734224925705249152	29870±250	5.76±0.02	-3.35±0.23	-33.5	35.04	14.45	sdB
198.942*	16.224036	424903052	3744601257454417152	32070±150	5.85±0.05	-2.04±0.05	16.3	45.27	15.79	sdOB
202.973147*	15.688212	142716122 [‡]	3744968013301724544	29370±250	5.53±0.04	-2.87±0.28	33.1	22.30	13.50	sdB
204.011629	36.091513	338308237	1471988375850922368	34250±300	5.91±0.05	-1.68±0.06	18.5	37.81	14.65	sdOB
204.70065*	-2.030358	212806164	3637481302758519040	32500±50	5.79±0.01	-2.91±0.08	84.9	131.58	13.39	sdB
205.036798*	47.864419	143413093 [‡]	1552221800914196480	28480±230	5.40±0.03	-2.70±0.10	27.5	28.45	13.58	sdB
212.567679*	32.412925	230113142	1478424229724415104	31620±340	6.03±0.06	-2.17±0.16	-36.7	12.06	14.90	sdB
212.607982*	-1.504604	449815203	3647329074356945152	36690±500	5.58±0.01	-2.85±0.12	99.3	46.77	13.72	sdOB
213.764081*	41.8243	575416138	1492192692285509376	30910±230	5.64±0.07	-2.93±0.23	35.3	27.02	14.79	sdB
216.283123*	20.378427	316812154	1240306604269576704	35660±450	5.72±0.08	-1.56±0.09	8.8	34.12	14.98	sdOB
217.123294*	21.10059	307805237	1240449403342559360	32550±80	5.86±0.03	-1.62±0.02	31.5	50.50	13.22	sdB
218.828893*	15.670621	148712144	1234322477875249664	26210±210	5.47±0.05	-2.52±0.10	95.1	22.46	13.86	sdB
220.220106*	-3.147965	132203002 [‡]	3648191164488514688	29490±260	5.45±0.03	-2.90±0.10	33.8	43.93	13.82	sdB
220.322231*	1.624409	527203236	3655309299687364992	29110±300	5.75±0.02	-2.38±0.11	30.5	53.88	14.26	sdB
223.665896*	19.616899	234115038	1237226700401153792	31000±140	5.88±0.02	-2.37±0.03	-55.7	64.13	12.45	sdB
225.102211*	42.095753	580111192	1585277243613047936	31000±130	5.59±0.03	-3.00>	99.7	105.90	13.88	sdB
230.1914*	29.80715	219416182	1275262415380252544	37890±480	6.03±0.07	-1.21±0.08	160.9	13.06	15.68	sdOB
232.708055*	6.015569	566509196	442911465952190080	33840±80	6.00±0.02	-1.45±0.03	15.2	67.63	14.71	sdOB
232.762545	33.638114	333013143	1373881186687373696	31680±190	5.92±0.04	-1.63±0.04	13.5	34.76	14.78	sdB
232.79329*	10.250305	243312195	1165963744033018496	26800±870	5.51±0.08	-2.47±0.11	24.2	19.02	13.57	sdB
233.317108*	44.587383	582404042	1394581623383963264	30400±150	5.80±0.03	-1.91±0.03	-107.0	56.07	15.54	sdB
233.456025*	37.991129	331509102	1375814952762454272	29300±120	5.55±0.01	-2.34±0.03	79.0	78.16	12.98	sdB
233.815317*	34.790072	322207235	1374058963973357696	38230±420	5.57±0.05	-3.44±0.34	17.3	26.53	15.05	sdB
235.097774*	26.808252	328611040	1223920926079402112	26220±120	5.41±0.04	-3.23±0.10	29.0	38.01	13.82	sdB
235.162647*	39.930281	152406202	1377891689708857856	33520±650	6.25±0.13	-3.00>	8.5	11.94	13.21	sdB
236.548706*	48.643679	155111084 [‡]	1401621384019650560	40900±320	6.27±0.07	4.01±0.06	70.1	19.56	12.79	He-sdB
237.701252*	16.440384	571812247	1196375273586921472	32050±60	5.68±0.04	-2.06±0.04	10.0	44.48	14.85	sdOB
240.300504*	53.197761	149514028 [‡]	1404827731724827776	30940±170	5.79±0.03	-2.44±0.06	86.4	31.64	14.25	sdB
240.380311*	4.674167 [†]	133105185 [‡]	4425487989169416320	38100±360	5.74±0.05	-0.38±0.02	-0.2	11.42	14.48	He-sdOB
242.015365*	7.074661	133011059 [‡]	4450489165598124800	32480±270	5.34±0.03	-2.54±0.09	32.7	26.69	12.83	sdB
242.478874	17.249217	447906246	1198927755470384128	29170±70	5.12±0.02	-0.47±0.03	-1.5	159.59	12.22	He-sdOB
242.838926*	52.768252	332203009	1427969118595251072	30870±190	5.66±0.04	-2.23±0.14	-35.8	78.27	12.77	sdB
243.002746*	51.82875	149505207 [‡]	1427678435208512384	34620±380	5.08±0.05	-3.00>	-37.4	25.11	13.67	sdOB
244.10151*	26.88743	574101201	1315765159572132224	44040±20	6.66±0.01	3.61±0.04	60.4	37.24	15.90	He-sdB
244.596204*	14.270251	337915062	4463625890008114944	36830±60	6.07±0.01	-1.45±0.02	17.0	58.18	13.44	sdOB
244.84679*	30.833913	220412139	1319053146015474688	36610±790	5.98±0.12	-1.50±0.12	11.6	16.18	15.63	sdOB
246.132846*	40.986953 [†]	241901157	1380974582874497280	28950±120	5.42±0.01	-2.48±0.04	28.4	87.55	14.46	sdB
246.818754*	40.457908 [†]	576301124	1332896306646572160	23710±60	5.49±0.01	-2.93±0.05	36.0	228.91	12.56	sdOB
247.093844*	27.488591 [†]	225003186	1305126525580012672	27750±180	5.42±0.03	-2.52±0.03	-40.3	107.87	13.64	sdB
248.005651*	7.994445 [†]	140315205	4440145853560129408	38450±840	5.42±0.01	-2.71±0.04	-47.4	63.05	12.87	sdO

Table 1. continued.

ra ^a	dec ^b	obsid ^c	source_id	T _{eff}	log g	log(nHe/nH) ^d	RV	SNRU	G	spclass
LAMOST	LAMOST	LAMOST	Gaia	(K)	(cm s ⁻²)		km s ⁻¹		Gaia(mag)	
251.154843*	-0.001554	340308108	4382904797178453504	26430±290	5.51±0.04	-2.59±0.06	88.3	25.03	13.66	sdB
252.2449*	24.967189	567901136	1300121926607765760	23390±370	5.72±0.04	-3.00>	27.0	17.52	16.07	sdB
252.499386*	53.525487	148415067‡	1425987175870116864	31000±740	5.60±0.12	-3.00>	35.5	15.11	14.02	sdB
253.928415*	13.030146	144307163	4449162845336419840	26230±550	5.34±0.06	-2.50±0.10	17.3	25.82	14.38	sdB
257.3859*	21.370697	575513248	4567834303554972288	35690±280	5.80±0.05	-1.40±0.05	14.6	23.45	15.61	sdOB
257.555047	53.446121	148413001	1419133610657016064	24010±440	5.54±0.11	-2.13±0.11	-55.5	14.11	12.60	sdB
258.078166*	48.976605	148506234‡	1414187320160273024	29870±170	5.85±0.05	-2.45±0.12	31.3	37.53	12.85	sdB
259.32832	42.435913	141008222	1360139937040515072	66410±10150	5.67±0.07	-2.88±0.43	3.7	31.96	12.48	sdO
260.35745*	9.053239	241603163	4491274930955326080	26640±490	5.55±0.04	-2.95±0.17	32.6	19.63	15.62	sdB
261.688678*	37.225178	462604059	1337242538672314112	36250±3050	5.86±0.47	-1.28±0.28	7.1	23.01	15.51	sdOB
261.989091*	25.143254	584512022	4570629777508086400	27540±390	5.47±0.07	-3.00>	106.3	11.43	12.99	sdB
264.126193*	7.600641†	341003194	4487346891305390528	27890±200	5.37±0.02	-3.14±0.12	56.5	26.28	13.70	sdB
264.360098*	22.149371	446111200	4557081835745623808	41170±590	5.28±0.02	-2.97±0.07	84.8	154.48	11.82	sdO
264.776732	11.296711	242308023	4492802221326659456	28430±160	5.52±0.02	-2.80±0.06	-107.9	67.02	13.30	sdB
265.091562*	48.899451	580907209	1363886900869046656	27550±290	5.41±0.03	-2.70±0.07	63.6	44.29	13.19	sdB
265.82931*	21.543762	457610044	4556063035156496768	37590±630	5.56±0.08	-2.42±0.13	153.8	16.01	14.01	sdOB
266.726507*	43.76783	568415057	1349088676950060672	33750±250	5.67±0.01	-1.66±0.04	13.7	67.95	14.38	sdOB
267.483551	0.110035	459005109	4371689194462064768	32600±100	5.89±0.01	-1.81±0.06	32.8	23.75	14.36	sdOB
268.270067	24.596209	457611042	4581048921494269056	37320±540	5.40±0.05	-3.07±0.26	10.2	18.09	14.61	sdB
272.388874	22.516659	234607117	4577984720030433536	27480±50	5.53±0.01	-2.62±0.03	29.2	43.85	12.94	sdB
279.443598*	59.26635	346815163	2154810316748450432	39210±70	5.72±0.05	-0.17±0.03	11.9	15.24	14.59	He-sdOB
285.754739	34.758065	574208088	2092525388221505792	28440±190	5.45±0.02	-2.97±0.05	33.3	47.26	15.69	sdB
285.90424*	38.603512	576405016	2100027626635533056	29050±120	5.39±0.03	-2.88±0.07	14.2	48.23	14.66	sdB
286.918867*	42.360115	161401152	2105469320138052668	30560±260	5.10±0.04	-1.59±0.04	9.2	136.24	10.59	sdB
287.27975*	37.937321	576407250	2099149567821051904	24320±90	5.42±0.02	-2.78±0.06	29.2	36.17	15.26	sdB
288.815187	43.674379	362008075	2103044549103238912	27850±240	5.57±0.04	-2.55±0.04	19.7	79.13	12.46	sdB
291.52478	47.254349	354204250	2129130844728397568	62190±140	5.65±0.07	0.00±0.04	26.2	62.45	14.86	He-sdO
291.539417*	37.335611	52401101	2051770507972278016	30670±160	5.82±0.05	-1.61±0.04	2.6	20.45	13.61	sdB
291.64212*	49.50824	353808152	2129777323205768448	27340±1140	5.56±0.13	-3.00>	94.2	13.85	14.80	sdB
294.635917*	46.066417	247615029	2080063931448749824	30030±80	5.43±0.02	-2.18±0.06	-37.3	109.98	12.14	sdB
294.82629	47.14856	354605098	2128554563197280512	29820±170	5.42±0.04	-2.32±0.10	30.9	19.83	15.40	sdB
296.05313	50.494251	354611122	2135353702585217920	27770±280	5.50±0.05	-2.31±0.08	149.9	21.90	15.48	sdB
297.984417*	46.130778	165903109	2079522048319286528	39380±420	5.51±0.03	-3.27±0.51	78.2	50.64	13.63	sdO
298.28497	47.716728	354606155	2086441927825846656	28810±300	5.42±0.05	-2.71±0.11	30.9	34.92	15.00	sdB
299.231536	43.837941	355101074	2079009641541181312	39060±180	5.72±0.04	-0.83±0.05	21.1	106.81	14.34	He-sdOB
300.179568	23.267099	577014004	1833281127895263872	35410±310	5.93±0.03	-1.45±0.03	77.0	74.30	11.97	sdOB
300.39346	44.574322	355208177	2076135724307679872	34260±1220	5.29±0.16	-2.75	-4.4	38.30	15.45	sdB
301.72862*	14.715003	462109242	1806906627074342016	34620±480	6.08±0.10	-1.60±0.09	14.7	10.48	14.34	sdOB
311.28078	36.636963	470909040	1870606730148932224	25040±180	5.79±0.04	-3.00>	37.1	15.36	16.48	sdB
312.413176	30.081818	475203139	1858674589447492608	37330±170	5.54±0.06	-2.58±0.12	20.2	98.43	13.50	sdOB
315.580451*	1.537663	370205063	1729653290822954880	34480±300	5.73±0.07	-1.43±0.05	8.3	47.99	15.00	sdOB
315.885216*	30.593842	475213199	1852616039853485824	34280±160	5.90±0.03	-1.77±0.03	10.6	63.82	12.95	sdOB
317.372429	13.279525	371607236	1758993857393963776	26520±450	5.52±0.06	-2.62±0.11	-38.0	25.36	15.42	sdB
317.672454*	14.433031†	371606237	1759968097711823232	43210±270	5.83±0.04	0.56±0.04	45.0	106.13	14.19	He-sdOB
318.417925*	20.715492	372014020	1789840488608448640	35220±310	5.29±0.03	-2.58±0.08	100.5	15.52	15.08	sdB
321.435002*	20.469909†	503309030	1790336673293954176	50130±380	5.57±0.04	0.20±0.04	5.2	64.56	13.37	He-sdO
322.335687	29.968578	368208087	1850084998438797312	34710±180	6.17±0.03	-1.76±0.04	79.5	70.36	14.10	sdOB
322.871071	19.865855	503313058	1787066145893240576	39960±710	5.94±0.02	-2.80±0.17	11.4	24.68	13.16	sdO
324.5772	34.351566	472809107	1950263255195349888	30340±180	5.41±0.03	-1.82±0.05	11.8	34.39	14.74	sdB
324.613116	46.192433	476303135	1977291346957976320	29330±300	5.80±0.09	-1.86±0.08	10.1	23.71	16.16	sdOB
324.833471	39.546916	172101139	1953965379566626816	46900±320	5.61±0.08	0.10±0.04	3.7	60.81	14.73	He-sdOB
325.278181	25.474982	471009116	1797986937760585600	43540±240	5.91±0.06	0.52±0.04	0.2	31.87	14.11	He-sdOB
325.676688	33.081334	472808084	1946937541760735872	35950±550	5.69±0.11	-1.36±0.09	14.0	39.62	14.79	sdOB
326.501298	37.35549	473209201	1952553606634620928	51430±360	5.74±0.08	0.16±0.05	74.4	31.05	14.66	He-sdO
330.2594*	8.513191	256811238	2724882872133120512	65560±1450	5.83±0.04	0.06±0.05	99.5	70.70	13.13	He-sdO
332.511298	25.066193	164209157	1879544900675463552	21290±80	5.32±0.02	-2.39±0.04	32.9	71.00	12.83	sdB
339.4026*	22.73709	490614158	1874534323107953664	42390±890	5.40±0.03	-3.09±0.10	31.3	83.68	12.76	sdO
340.718491*	1.872661	362211238	2654793575707334784	31140±90	5.93±0.02	-2.36±0.04	-108.9	58.30	14.44	sdB
340.871872*	10.781563	157006179	2717582699040219392	34270±180	5.77±0.04	-1.57±0.04	16.2	87.75	15.04	sdOB
341.890375*	31.325914	264909113	1889631201873127424	28940±240	5.55±0.04	-2.63±0.12	29.4	43.26	15.45	sdB
343.992447*	33.719939	370916040	1891098500140100352	28650±270	5.64±0.07	-2.86±0.17	35.1	12.05	12.77	sdB
344.15977*	6.947541	256106208	2712047826225618048	29920±270	5.65±0.05	-2.79±0.13	-40.4	42.85	15.26	sdB
345.4409*	13.64374	363809200	2815153223450428032	31190±220	5.73±0.04	-1.74±0.04	26.5	79.42	14.52	sdB
346.401764*	34.698363	164306246	1914301803258669440	28260±160	5.50±0.01	-2.34±0.03	14.2	72.89	13.29	sdB
347.375115*	28.568276	470009143	2845710850610464640	31890±160	5.73±0.03	-1.72±0.03	12.9	76.25	14.48	sdOB
349.980633*	4.876289	56601022	2660835289023309696	41390±2960	6.23±0.23	-3.24±1.06	143.2	11.20	12.81	sdB
351.114427*	21.647578	260216070	2837982520817733376	41900±40	6.05±0.04	0.98±0.06	42.0	48.53	13.74	He-sdOB
355.0197*	7.285939	361504161	2757157489778320000	30720±190	5.93±0.07	-1.88±0.04	15.9	95.88	13.47	sdB
358.822256*	18.337599	54914220‡	2774038154361038976	47080±950	5.44±0.13	0.53±0.10	2.2	21.80	13.32	He-sdOB

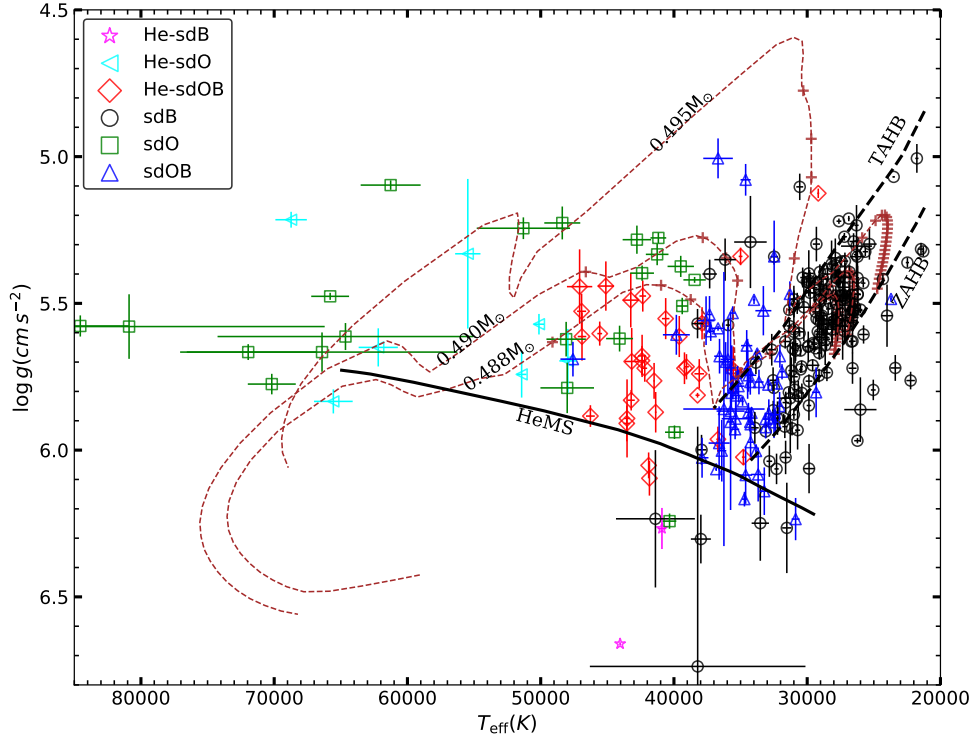


Figure 6. $T_{\text{eff}}\text{-log } g$ diagram for the 294 hot subdwarf stars identified in our study. He-sdB, He-sdO, He-sdOB, sdB, sdO and sdOB stars are represented by magenta stars, aqua left triangles, red diamonds, black circles, green squares and blue up triangles, respectively. The thick solid line denotes the He-MS, which is taken from Paczyński (1971), while the two dashed line represent the ZAHB and TAHB from Dorman et al. (1993) for $[\text{Fe}/\text{H}]=-1.48$. Three sdB evolution tracks from Dorman et al. (1993) for $[\text{Fe}/\text{H}]=-1.48$ are added, which are denoted by brown dashed lines. The stellar masses at the ZAHB are labeled close to each track. The time interval between two adjacent + markers is 5 Myr.

3.2. Parameter diagram

In Fig 6, we present the $T_{\text{eff}}\text{-log } g$ diagram for the identified 294 hot subdwarf stars. The two dashed lines in the figure are the zero-age HB (ZAHB) and terminal-age HB (TAHB) calculated by Dorman et al. (1993) for $[\text{Fe}/\text{H}]=-1.48$, while the solid line denotes the He main-sequence (He-MS) from Paczyński (1971). The three brown dashed curves mark three sdB evolution tracks for $[\text{Fe}/\text{H}]=-1.48$, which are from Dorman et al. (1993), and the time interval between two adjacent + marks is 5 Myr. The stellar masses at ZAHB are also labeled close to each track. He-sdB, He-sdO, He-sdOB, sdB, sdO and sdOB stars are represented by different colors and marks, respectively.

It is clear from Fig 6 that most of the sdB stars (i.e., black circles) settle in the region well defined by the ZAHB and TAHB lines, and they cluster near near $T_{\text{eff}} = 29\,000$ K and $\log g = 5.5\text{ cm s}^{-2}$. Similarly, most of sdOB stars (i.e., blue up triangles) are located in the area between the ZAHB and TAHB as well, but they present a little higher temperatures and gravities than sdB stars, which cluster near the position of $T_{\text{eff}} = 34\,000$ K and $\log g = 5.8\text{ cm s}^{-2}$. On the other hand, nearly all of the He-sdOB stars (red diamonds) are located above the TAHB and center at the position of $T_{\text{eff}} = 40\,000$ K and $\log g = 5.6\text{ cm s}^{-2}$, while sdO stars (i.e., green squares) and He-sdO (i.e., aqua left triangles) present a much more dispersive distribution in $T_{\text{eff}}\text{-log } g$ diagram and higher temperatures than other type of hot subdwarf stars (e.g., some of them have $T_{\text{eff}} > 60\,000$ K).

Fig 7 shows the $T_{\text{eff}}\text{-log}(n\text{He}/n\text{H})$ diagram for the hot subdwarf stars in our sample. The different types of hot subdwarf stars are denoted by the same markers as in Fig 6. The red horizontal dashed line in this figure represents the solar He abundance (e.g., $\log(n\text{He}/n\text{H}) = -1$). As described by other authors (e.g., Edelmann et al. 2003; Németh et al. 2012; Geier et al. 2013; Luo et al. 2016), two distinct He sequences can be outlined in Fig 7 clearly. The black dotted line and black solid line are the linear regression lines found by Edelmann et al. (2003) to fit the He-rich and

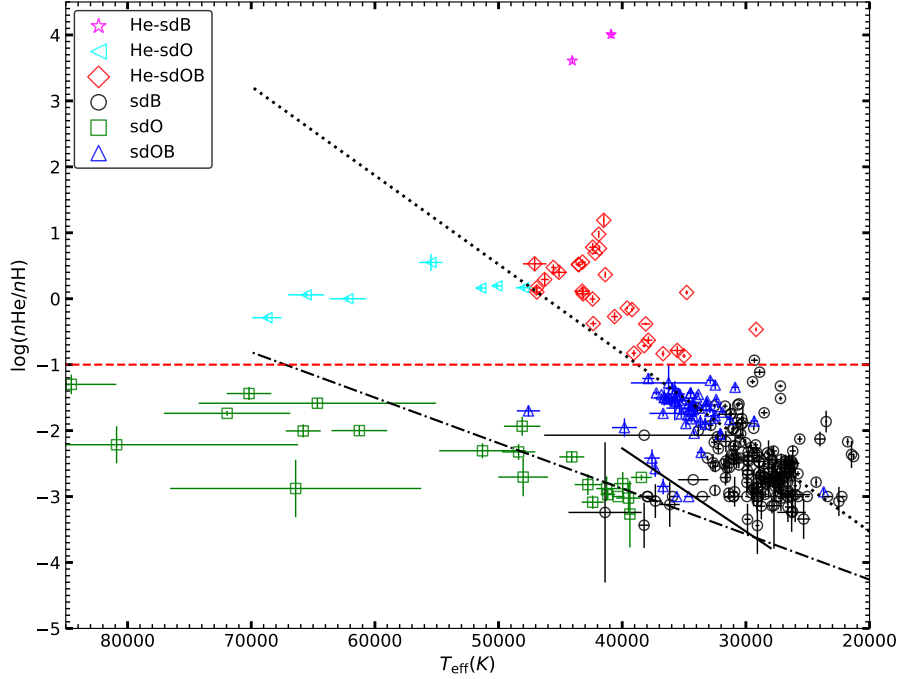


Figure 7. $T_{\text{eff}}\text{-}\log(n\text{He}/n\text{H})$ diagram for the 294 hot subdwarf stars identified in our study. Different types of hot subdwarf stars are denoted by the same markers as in Fig 6. The red dashed line denotes the solar He abundance. The dotted line and solid line are the linear regression line fitted by Edelmann et al. (2003), while the dot-dashed line is the best-fitting line for the He-weak sequence in Németh et al. (2012).

He-weak sequence in their study respectively, and they are described by the following equations:

$$\log(n\text{He}/n\text{H}) = -3.53 + 1.35 \left(\frac{T_{\text{eff}}}{10^4 K} - 2.00 \right), \quad (1)$$

$$\log(n\text{He}/n\text{H}) = -4.79 + 1.26 \left(\frac{T_{\text{eff}}}{10^4 K} - 2.00 \right). \quad (2)$$

Németh et al. (2012) used another linear regression line to fit the He-weak sequence in a larger parameter space, which is described by the following equation,

$$\log(n\text{He}/n\text{H}) = -4.26 + 0.69 \left(\frac{T_{\text{eff}}}{10^4 K} - 2.00 \right). \quad (3)$$

This linear regression line is also presented by a black dot-dashed line in Fig 7. Fig 7 shows that both the He-rich and He-weak sequences show an increasing He abundance with temperature. Moreover, our He-rich sequence consists of sdB (black circles), sdOB (blue triangles), He-sdOB (red diamonds), He-sdO (aqua left triangles) and He-sdB (magenta) stars. Moreover, sdB stars have their He abundance in the rough range of $-4 < \log(n\text{He}/n\text{H}) < -2$, sdOB stars have their He abundance in the rough range of $-2 < \log(n\text{He}/n\text{H}) < -1$, and most of He-sdOB stars are in the rough He abundance range of $-1 < \log(n\text{He}/n\text{H}) < 2$. He-sdO stars have similar He abundances as He-sdOB stars in our sample, but they present higher temperatures than He-sdOB stars. We have 2 He-sdB stars (magenta stars), which present the highest He abundance in our sample. Our He-rich sequence could be approximately fitted by the line found by Edelmann et al. (2003). The He-weak sequence consists of all sdO stars and a few of sdB and sdOB stars with very low He abundance. Furthermore, the He-weak sequence is quite diverse and better reproduced by the fitting line used in Németh et al. (2012) than the one used in Edelmann et al. (2003).

We show the $\log g\text{-}\log(n\text{He}/n\text{H})$ diagram for our identified hot subdwarf stars in Fig 8. Like in Fig 6 and 7, different types of hot subdwarf stars are denoted by different markers, and the red dashed line is the solar He abundance (e.g., $\log(n\text{He}/n\text{H}) = -1$). In this figure, no distinct sequences are presented and, in general, all hot subdwarf stars independent of their spectral types show a wide distribution of surface gravities.

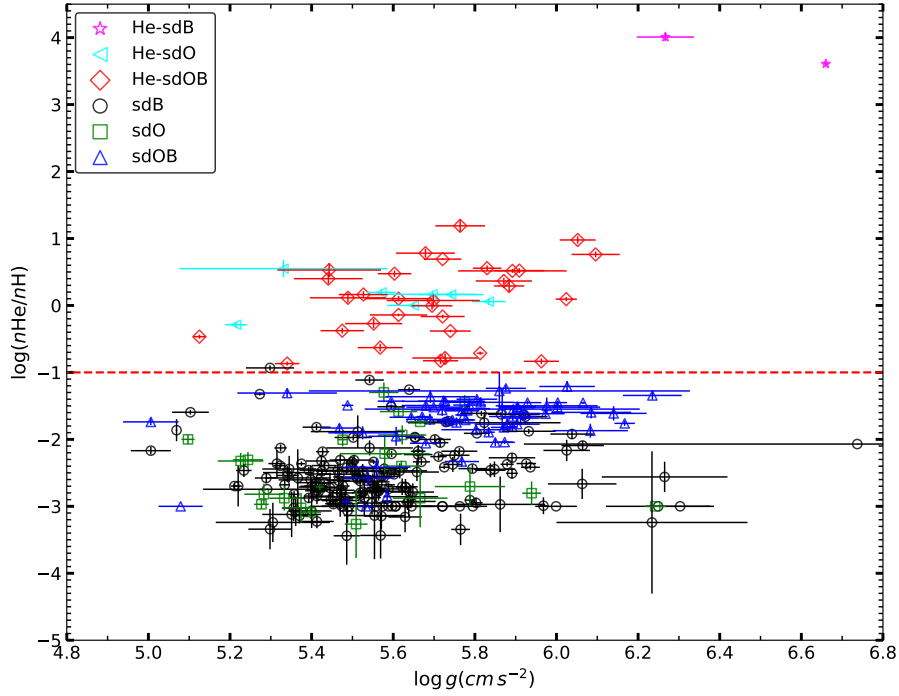


Figure 8. $\log g$ - $\log(n\text{He}/n\text{H})$ diagram for the 294 hot subdwarf stars identified in our study. The red dashed line denotes the solar He abundance. Different types of hot subdwarf stars are denoted by the same markers as in Fig 6.

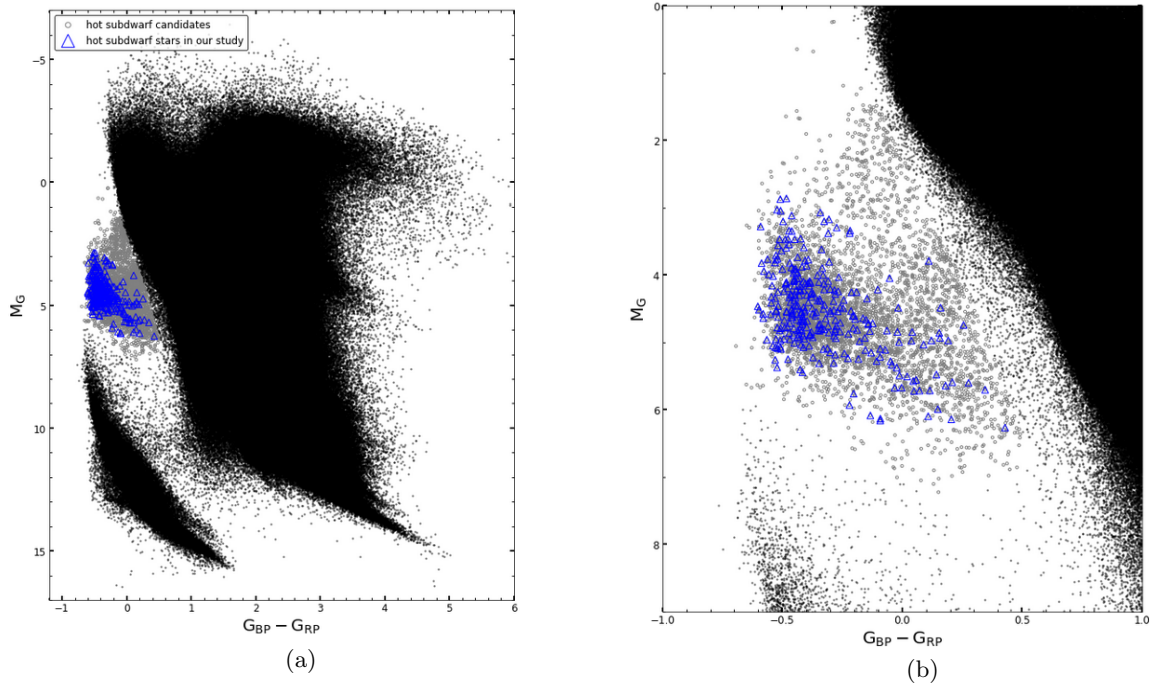


Figure 9. Panel (a) : Gaia HR diagram. Hot subdwarf candidates (e.g., 4593 objects) are marked with gray circles. 294 hot subdwarf stars confirmed in our study are marked with blue triangles. Panel (b) : Magnified drawing for hot subdwarf region.

4. DISCUSSION AND SUMMARY

With the accurate astrometry and photometry from Gaia DR2, it is now possible to build a HR diagram with huge number of homogeneous data (Gaia collaboration et al. 2018b), which eventually provide us a new tool to study stellar

evolution for the stars at different evolutionary stages. Panel (a) of Fig 9 shows the hot subdwarf stars identified in the Gaia DR2 HR diagram (Gaia collaboration et al. 2018b, see Section 2.1 for details). The gray dots within the polygon are the hot subdwarf candidates (i.e., 4593 stars) selected in our study (see Section 2), while the blue triangles are the hot subdwarf stars identified in our study. Panel (b) of Fig 9 is the magnified region where we selected the hot subdwarf candidates.

Fig 9 shows clearly that the majority of hot subdwarf stars are found at the typical position where they are expected in the HR diagram, e.g., clustering at $M_G \approx 5$ and $BP-RP \approx -0.2$. However some stars with a spectroscopic subdwarf confirmation appear far from the subdwarf region, e.g., a few of stars extend the hot subdwarf distribution to the right and connect it with the wide MS. Some of these stars are hot subdwarf binaries with a WD or low mass MS companion (a detailed study for the hot subdwarf binaries are out of the scope of this work), while some spectra may suffer from the effects of unknown extinction (Andrae et al. 2018) and present redder positions in the HR diagram than normal hot subdwarf stars.

We have selected 4593 hot subdwarf candidates by means of the Gaia DR2 HR diagram, among which more than 700 objects have spectra in LAMOST DR5. Finally, we confirmed 294 hot subdwarf stars from our candidates, including 169 sdB, 63 sdOB, 31 He-sdOB, 22 sdO, 7 He-sdO and 2 He-sdB stars. Considering hot subdwarfs that are not listed in Geier et al 2017 as new discoveries, we found 110 new hot subdwarfs in our study. Note however, that besides the hot subdwarf candidates which have LAMOST spectra, there are more than 3800 candidates without spectra in LAMOST, and most of them are likely real hot subdwarf stars based on their positions near the hot subdwarf region in Gaia HR diagram. In future work we will use LAMOST to obtain the spectra of these candidates, which will eventually help us obtain their atmospheric parameters and spectral classification types. On the other hand, the samples which were used to built the HR diagram in Gaia collaboration et al. (2018b) have only the most precise parallaxes and photometry. These samples represent only the tip of the iceberg. We hope to find many more hot subdwarf stars by combining the LAMOST spectroscopic database with the whole Gaia DR2 source list.

This work is supported by the National Natural Science Foundation of China Grant Nos 11390371, 11503016 and U1731111, Natural Science Foundation of Hunan province Grant No.2017JJ3283, the Youth Fund project of Hunan Provincial Education Department Grant No.15B214, the Astronomical Big Data Joint Research Center, co-founded by the National Astronomical Observatories, Chinese Academy of Sciences and the Alibaba Cloud. This research has used the services of www.Astroserver.org under reference X074VU and KS5NVO. P.N. acknowledges support from the Grant Agency of the Czech Republic (GAČR 18-20083S). The LAMOST Fellowship is supported by Special Funding for Advanced Users, budgeted and administered by the Center for Astronomical Mega-Science, Chinese Academy of Sciences (CAMS). Guoshoujing Telescope (the Large Sky Area Multi-Object Fiber Spectroscopic Telescope LAMOST) is a National Major Scientific Project built by the Chinese Academy of Sciences. Funding for the project has been provided by the National Development and Reform Commission. LAMOST is operated and managed by the National Astronomical Observatories, Chinese Academy of Sciences.

REFERENCES

- Arenou, F., Luri, X., Babusiaux, C., et al. 2018, arXiv:1804.09375
- Andrae, Rene., Fouesneau, Morgan., Creevey, Orlagh., et al. 2018, arXiv:1804.09374
- Bu, Yude., Lei, Zhenxin., Zhao, Gang., et al. 2017, ApJS, 233, 2
- Chen, Xuefei., Han, Zhanwen., Deca, Jan., et al. 2013, MNRAS, 434, 186
- Copperwheat, C. M., Morales-Rueda, L., Marsh, T. R., et al. 2011, MNRAS, 415, 1381
- Cui, Xiang-Qun., Zhao, Yong-Heng., Chu, Yao-Quan., et al. 2012, RAA, 12, 1197
- Dorman, Ben., Rood, Robert T., & O’Connell, Robert W. 1993, ApJ, 419, 596
- Edelmann, H., Heber, U., Hagen, H.-J., et al. 2003, A&A, 400, 939
- Gaia Collaboration, Brown, A., Vallenari, A., et al. 2018a, arXiv:1804.09365
- Gaia Collaboration, Babusiaux, C., van Leeuwen, F., et al. et al. 2018b, arXiv:1804.09378
- Geier, S., Hirsch, H., Tillich, A., et al. 2011, A&A, 530, 28
- Geier, S., Heber, U., Edelmann, H., et al. 2013, A&A, 557, 122
- Geier, S., Østensen, R. H., Nemeth, P., et al. 2017, A&A, 600, 50

- Green, R. F., Schmidt, M., Liebert, J. 1986, *ApJS*, 61, 305
- Heber, U. 2009, *ARA&A*, 47, 211
- Heber, U. 2016, *PASP*, 128, 2001
- Han, Z., Podsiadlowski, Ph., Maxted, P. F. L., et al. 2002, *MNRAS*, 336, 449
- Han, Z., Podsiadlowski, Ph., Maxted, P. F. L., et al. 2003, *MNRAS*, 341, 669
- Han, Z., Podsiadlowski, Ph., & Lynas-Gray, A. E. 2007, *MNRAS*, 380, 1098
- Hubeny, I., & Lanz, T. 2017, [arXiv:1706.01859](https://arxiv.org/abs/1706.01859)
- Jenkins, Edward B. 2013, *ApJ*, 764, 25
- Lanz, Thierry., & Hubeny, Ivan. 2007, *ApJS*, 169, 83
- Lei, Zhenxin., Chen, Xuemei., Zhang, Fenghui., et al. 2015, *MNRAS*, 449, 2741
- Lei, Zhenxin., Zhao, Gang., Zeng, Aihua., et al. 2016, *MNRAS*, 463, 3449
- Lindgren, L., Hernandez, J., Bombrun, A., et al. 2018, [arXiv:1804.09366](https://arxiv.org/abs/1804.09366)
- Luo, Yang-Ping., Németh, P., Liu, Chao., et al. 2016, *ApJ*, 818, 202
- Maxted, P. F. L., Heber, U., Marsh, T. R., et al. 2001, *MNRAS*, 326, 139
- Michaud, G., Richer, J., Richard, O. 2008, *ApJ*, 675, 1223
- Michaud, G., Richer, J., Richard, O. 2011, *A&A*, 529, 60
- Napiwotzki, R., Karl, C. A., Lisker, T., et al. 2004, *Ap&SS*, 291, 321
- Németh, P., Stenzen, R., Tremblay, P., et al. 2014, *ASPC*, 481, 95
- Németh, P., Kawka, A., & Vennes, S. 2012, *MNRAS*, 427, 2180
- O'Connell, Robert W. 1999, *ARA&A*, 37, 603
- Paczyński, B. 1971, *Acta Astron*, 21, 1
- Vennes, S., Kawka, A & Németh, P. 2011, *MNRAS*, 410, 2095
- Xiong, H., Chen, X., Podsiadlowski, Ph., et al. 2017, *A&A*, 599, 54
- Xue, X. X., Rix, H. W., Zhao, G., et al. 2008, *ApJ*, 684, 1143
- York, Donald G., Adelman, J., Anderson, John E., et al. 2000, *AJ*, 120, 1579
- Zhang, Xianfei., & Jeffery, C. S. 2012, *MNRAS*, 419, 452
- Zhang, Xianfei., Hall, Philip D., Jeffery, C. Simon., et al. 2017, *ApJ*, 835, 242
- Zhao, Gang., Chen, Yu-Qin., Shi, Jian-Rong., et al. 2006, *ChJAA*, 6, 265
- Zhao, Gang., Zhao, Yong-Heng., Chu, Yao-Quan., et al. 2012, *RAA*, 12, 723